Supplement of Atmos. Chem. Phys., 24, 3421–3443, 2024
https://doi.org/10.5194/acp-24-3421-2024-supplement

Supplement of

Observations of cyanogen bromide (BrCN) in the global troposphere and their relation to polar surface O_3 destruction

James M. Roberts et al.

Correspondence to: James M. Roberts (james.m.roberts@noaa.gov)

Supplement to: BrCN in the global troposphere

S1 Formation of BrCN from HOBr chemistry

The formation of XCN compounds from reactions of HCN/CN^- in the condensed phase is well known, so deserves consideration in the context of the polar boundary layer. The major sources of HCN to the atmosphere are biomass burning and vehicle exhaust, two sources that favor the northern hemisphere. HCN is a very weak acid (pKa=9.4), is not very soluble in water (Yoo et al., 1986), and its gas phase loss processes are quite slow (several years against reaction with OH). Consequently, HCN is widely distributed throughout the troposphere as is apparent in the ATom data shown in the main text. Vertical profiles of HCN imply a surface sink and the effective lifetime of HCN has been estimated to be about 5 months (Li et al., 2003). The data from ATom-3&4, including the vertical profile and inter-hemisphere distribution, are for the large part in agreement with this.

There are many parameters that go into a model description of polar bromine chemistry, some of them fairly uncertain (for example rate constants at cold temperatures). One way to isolate and examine how BrCN formation from HCN might impact the active-bromine cycle is to compare the rates of liquid phase chemistry that perpetuates the Br cycle, to the chemistry that would remove active Br by making BrCN (Gerritsen et al., 1993):

$$Br_2 + HCN \rightarrow BrCN + Br^- + H^+ \qquad (k = 800\ M^{-1}s^{-1}) \qquad (S1)$$

$$HOBr + HCN \rightarrow BrCN + H_2O \qquad (k = 10\ M^{-1}s^{-1}) \qquad (S2)$$

$$OBr^- + CN^- + H_2O \rightarrow BrCN + 2OH^- \qquad (k = 5.7 \times 10^7\ M^{-1}s^{-1}) \qquad (S3)$$

$$HOBr + CN^- \rightarrow BrCN + OH^- \qquad (k = 4.2 \times 10^9\ M^{-1}s^{-1}) \qquad (S4)$$

So, the formation of BrCN from HCN is highly pH dependent, slower at lower pHs. This is a result both of the slower rate constants of the parent compounds compared to the conjugate anions, and the lower solubility of HCN (pKa=9.4) at atmospheric pHs. The main liquid-phase reactions of HOBr that perpetuate the bromine explosion are the acid-assisted mechanism (Roberts et al., 2014):

$$HOBr + X^- \leftrightarrow HOBrX^- \qquad k_1, k_{-1} \qquad (S5)$$

$$HOBrX^{-} + H^{+} \rightarrow H_2O + BrX \qquad k_H \qquad (S6)$$

$$HOBrX^{-} \rightarrow OH^{-} + BrX \qquad k_0 \qquad (S7)$$

$$k^{II} = \{k_1(k_0 + k_H[H^+])\}/\{k_{-1} + k_0 + k_H[H^+]\} \qquad (EqS1)$$

and are also pH dependent, but in the opposite sense. For Br_2/HOBr/OBr^{-} reacting with HCN/CN^{-} be a significant source of BrCN reactions S1-S4 would have to compete with reactions S5-S7 in the liquid (liquid-like or quasi-liquid layer) phase.

The rates of HOBr reaction that leads to BrCN formation can be estimated based on the above rate constants and pH dependencies, and measured ambient HCN mixing ratios (range 100 to 500 pptv). The liquid phase concentrations of HCN/CN^{-} as a function of pH can be estimated from the intrinsic Henry's Law solubility of HCN (H*), recognizing that for a weak acid the effective Henry's Law solubility (H_{eff}) is given by:

$$H_{eff} = H^*(1+K_a/[H^+]) \qquad (EqS2)$$

where K_a is the acid dissociation constant for HCN, and H_{eff} and H* have units of M/atm (Sander, 2015). The intrinsic solubility of HCN as a function of temperature shows the expected inverse exponential relationship with temperature (Fig. S23) and for the purposes of this work, we will assume that this relationship can be extrapolated to temperatures as low as 263K. This H*(T), Equation (2), and the acid dissociation of HCN are used to estimate [HCN] and [CN^{-}] assuming equilibrium with ambient HCN, and the acid dissociation of HOBr (pKa =8.6) along with the rates of S(2-4) give the estimated loss rates of HOBr (d[HOBr]/[HOBr]/dt) as a function of pH shown in Fig. S24.

The competing reactions of HOBr with $Br^{-}$and Cl^{-} as a function of pH can also be estimated from the acid dissociation of HOBr and the rates of R1&S5, assuming the surface concentrations of Cl^{-} and Br^{-} are the range measured in surface snow in the Arctic, 16µM (see for example (Domine et al., 2004)). It should be noted that Cl^{-} and Br^{-} in the range used in this model are at the low end of the distributions measured in sea ice and sea salt-impacted environments (Domine et al., 2004;Krnavek et al., 2012;Dibb et al., 2010). The results of those estimates are also shown in Fig. S24, and have the opposite relationship with pH. The two pathways are of equal importance somewhere around pH=7, however, considering the uncertainties of the above analysis, a range of pH=6-8 is probably more realistic. The presence of higher Br^{-} (and Cl^{-}) concentrations on the reaction substrate, like those referenced above, would serve to shift the pH at which BrCN becomes favorable to slightly higher values.

S1.1 Multiphase Experiments

The NOAA group conducted several experiments on the simple multiphase chemistry of BrCN formation and to determine if reactions of BrCN with bromide in aqueous solution could reform active-Br, Br_2 in particular. These tests were conducted with a quadrupole I-CIMS that had generally lower sensitivity to Br_2 and BrCN than the ToF CIMS (Br_2 DL = 140 pptv and BrCN DL = 30 pptv for 10sec averages). The instrument was calibrated using a gravimetrically-calibrated Br_2 permeation tube and with the BrCN diffusion source described in the main text. Preliminary lab tests were conducted to examine the temperature and pH dependence of the Br_2 + HCN chemistry on ice/water surfaces, and confirmed the absence of BrCN production in the absence of a high pH aqueous surface on which it can take place. In those tests, combining Br_2 (28ppbv) and HCN (5 ppbv) in the PFA Teflon inlet of that instrument (0.4cm ID, 2m length, 2.20 slpm flow of room air at 30% RH) produced no BrCN above detection limit. Substantial production of BrCN was apparent when Br_2 and HCN were reacted in a high-surface area reactor (Roberts and Liu, 2019) containing a small amount of liquid water at pH8, qualitatively confirming the chemistry proposed in this work. The experiments aimed at determining if BrCN could reform active Br upon reaction with bromide ions in solution were conducted with an apparatus similar to that described previously (Roberts et al., 2009). In those tests, a stream of BrCN (up to 150 ppbv) in zero air, at flow rates in the range 100 – 200 SCCM, was passed over a slurry of NaBr in water, and the effluent was measured with the I-CIMS. There was no detectable Br_2 formed, leading to an upper limit of about 0.1% conversion of the BrCN stream.

S2 Box Model

The basic box model used to assess possible BrCN formation has described previously (Wang and Pratt, 2017). The chemistry from Reactions S1–4 and the pH dependent solubility of HCN (Equation S2) were added to the model and the conditions found during the 4/27/2018 MA were used to initialize the model. The results of the model, shown in Fig. S25, show the same pH dependence from the HOBr competitive reaction analysis. The absolute amount of BrCN is lower than observed, however it should be noted that loss rates and mechanisms of BrCN in this environment are currently unknown.

Figures

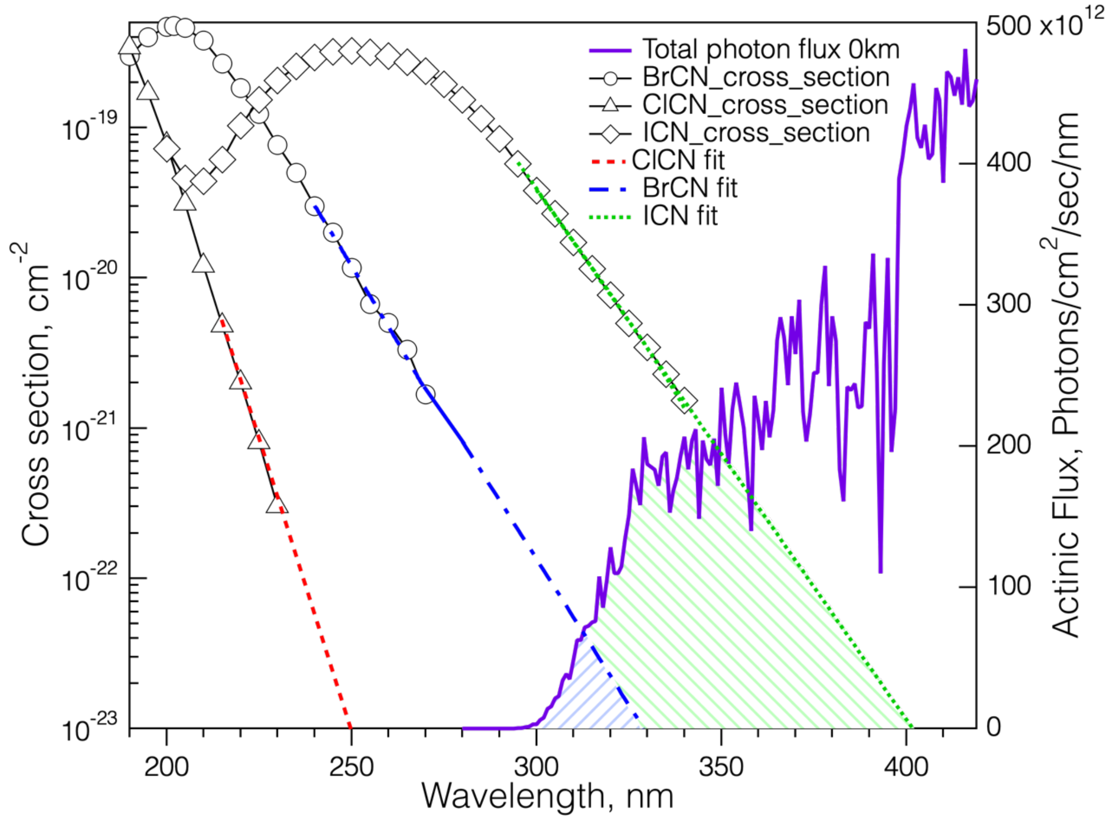

Figure S1. The UV-visible absorption spectra of ClCN, BrCN, and ICN, (Felps et al., 1991;Barts and Halpern, 1989;Russell et al., 1987;Hess and Leone, 1987), and the photon flux spectrum estimated from the NCAR TUV model for 40° N, at the surface on June 30, 2015 (NCAR, 2018). The extrapolations assume the cross-sections are log-linear over the portions that tail into the actinic region. The cross-hatched shaded areas denote the regions in which BrCN and ICN overlap with the solar flux.

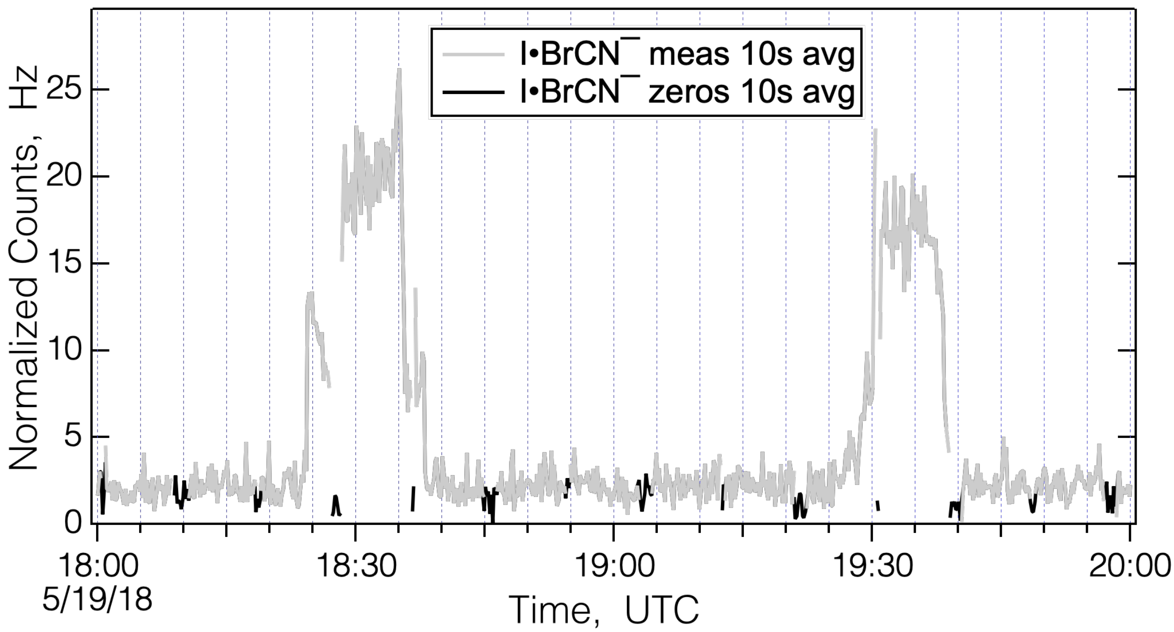

Figure S2. The time series of I^{79}BrCN^{-} signals measured during the 5/19/18 flight over the Arctic. The grey lines are measurements of ambient air and the black lines are measurements during times the inlet was over-flowed with scrubbed air.

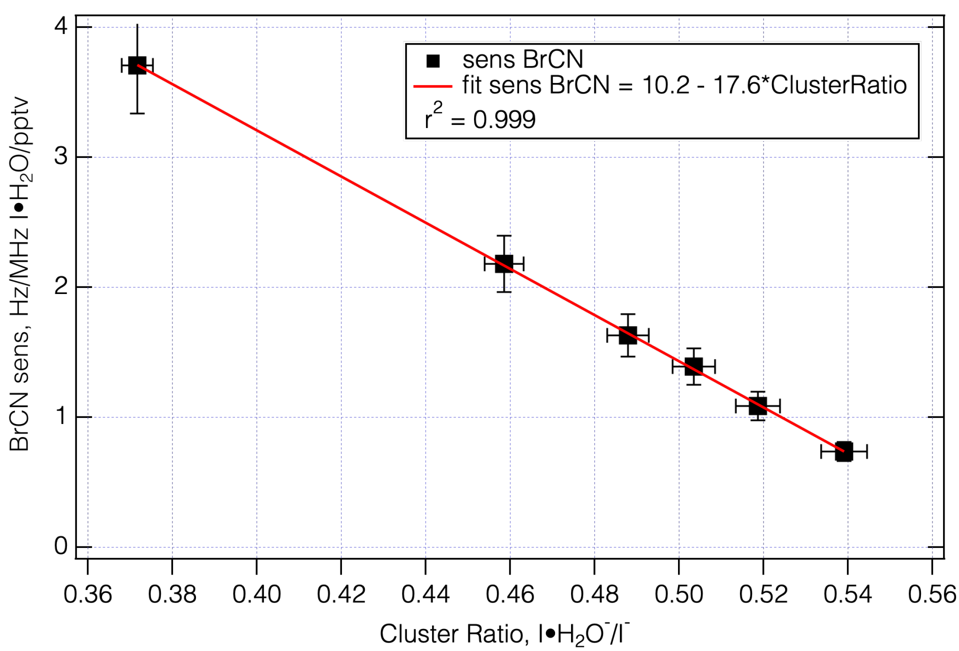

Figure S3. The water vapor dependence of I-CIMS sensitivity to BrCN.

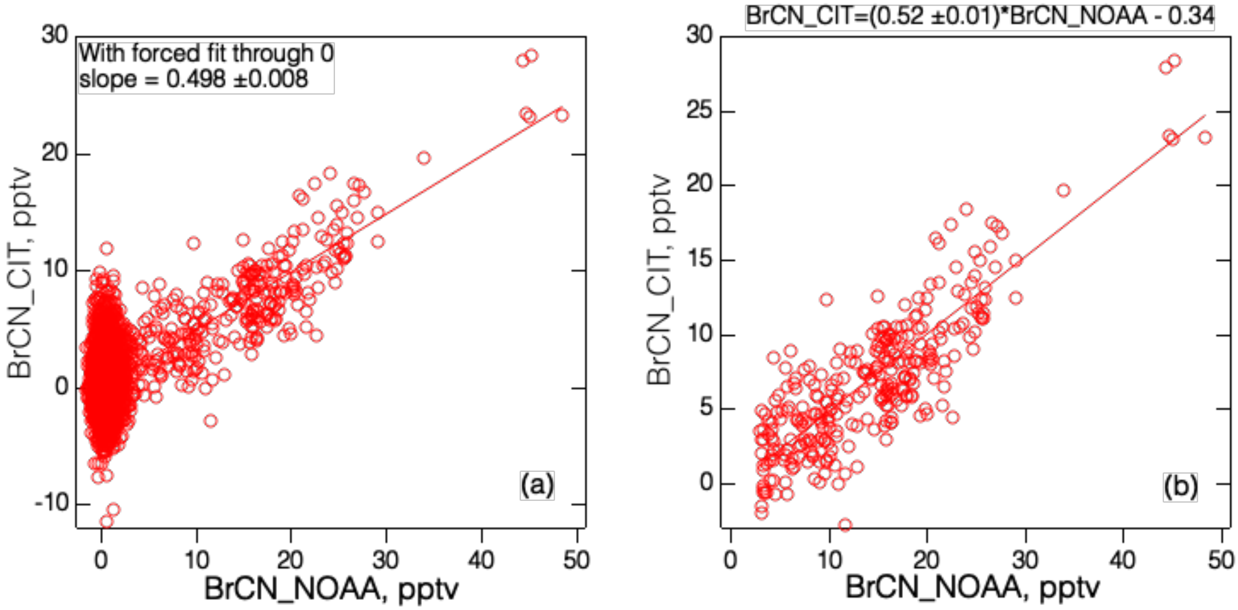

Figure S4. Plots of CIT-CIMS BrCN versus I-CIMS BrCN for both Apr. 27, 2018 and May 19, 2018 flights during ATom-4 as originally calibrated by each group. Panel (a) includes all the data and panel (b) includes only the data for which the I-CIMS BrCN was above 3 pptv. The fit line in panel (b) is from an ODR that assumes uncertainty in each variable.

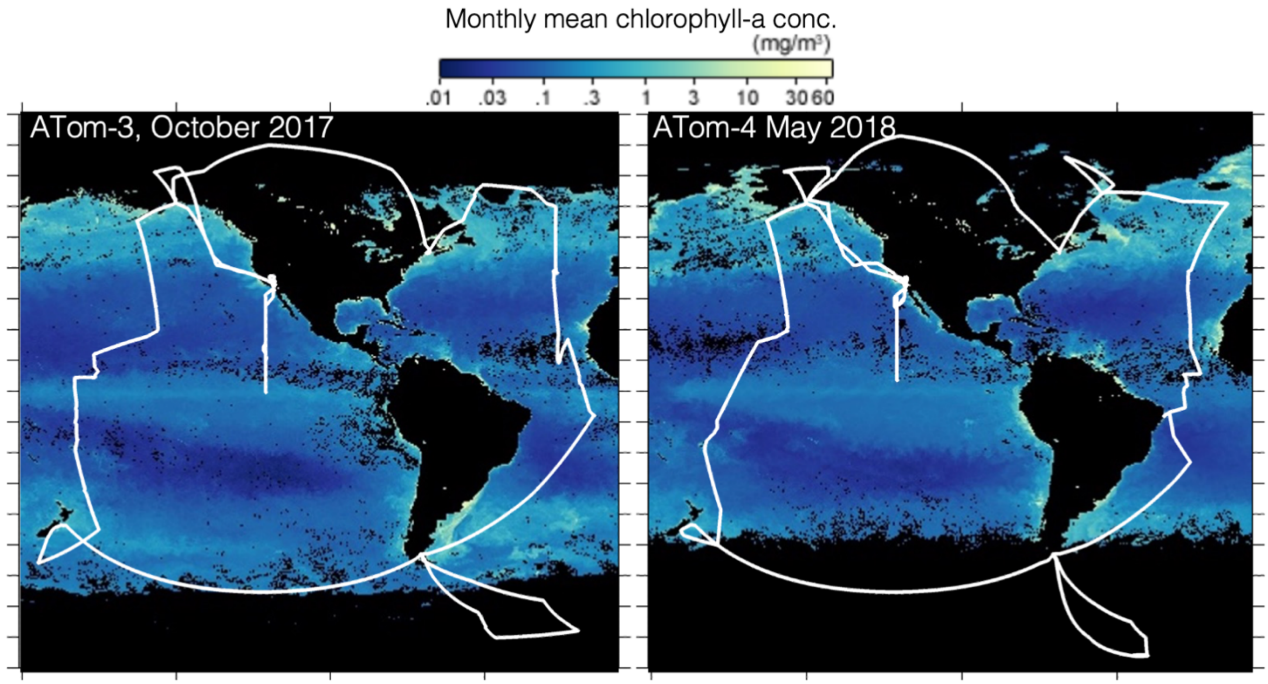

Figure S5. Maps of surface chlorophyll α concentrations estimated from satellite observations (https://neo.gsfc.nasa.gov/view.php?datasetId=MY1DMM_CHLORA) for the main months of the ATom-3 (right panel) and ATom-4 (left panel) deployments. The black regions are either areas that had too much ice cover to permit a retrieval, or are land masses.

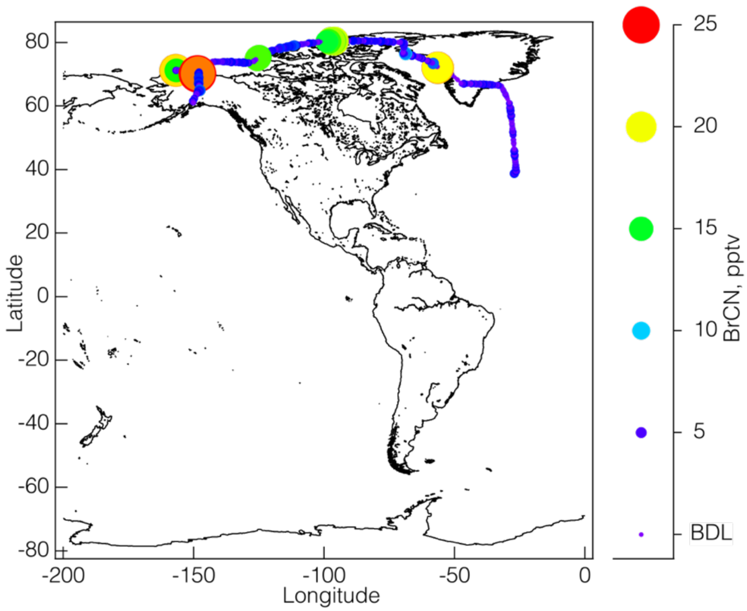

Figure S6. The map of BrCN mixing ratios (60s avg) observed during the Feb 18 and Feb 19, 2017 flights during ATom-2.

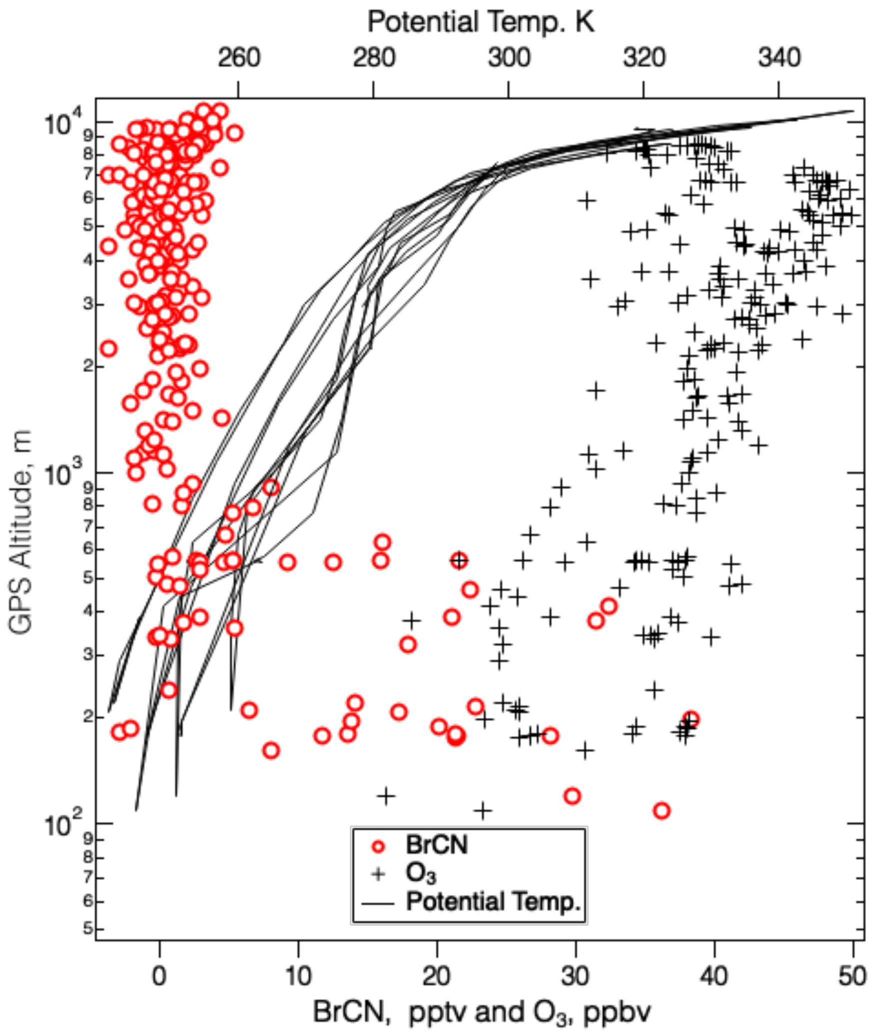

Figure S7. The ATom-2 BrCN and O_3 measurements as a function of altitude for both Arctic flights. The measurements were averaged over the UCI-WAS sample time to be compatible with the data in Fig. 4 in the main text. The BrCN values are shown as red circles and the O_3 values are shown as black crosses, and the potential temperature measured during the flight is shown in black lines.

Figure S8. An image from the nose camera video of the DC-8 taken at 23:40:11 UTC during the low-level leg of the Oct. 11, 2017 flight described in the main text. The videos acquired on the aircraft were stored as .mkv files (https://asp-archive.arc.nasa.gov/), converted to .avi files via MATLAB and stored on Google Drive. The videos were then played directly by Document Viewer for Google Drive.

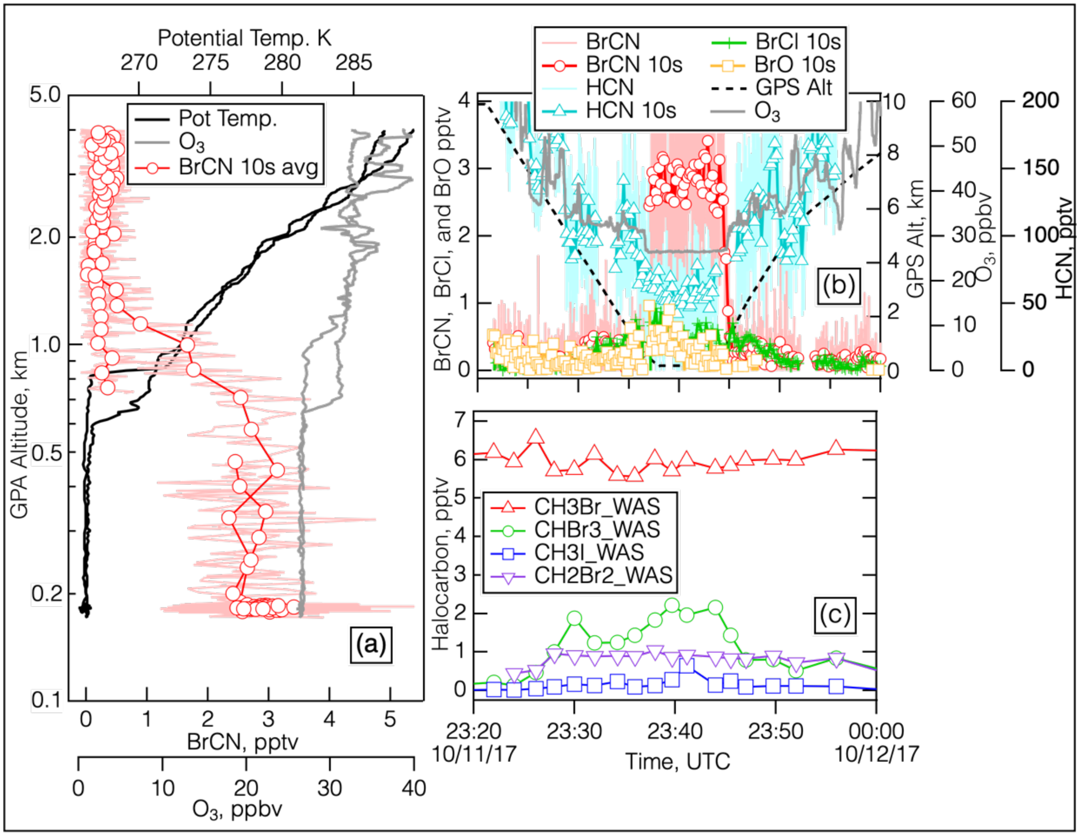

140

Figure S9. Details of the measurements during the polar boundary layer leg of the Oct. 11, 2017 flight over the Southern Ocean at 65.26 S Lat., 124.4 W Long., centered around 23:40 UTC. The left panel are the altitude profiles of potential temperature, O_3 and BrCN (10 s avg). The top right panel shows the time series for BrCN, BrCl, BrO, HCN, O_3, and altitude. The bottom right panel shows the time series for the halocarbons, CH_3Br, CH_3I, CH_2Br_2 and $CHBr_3$.

145

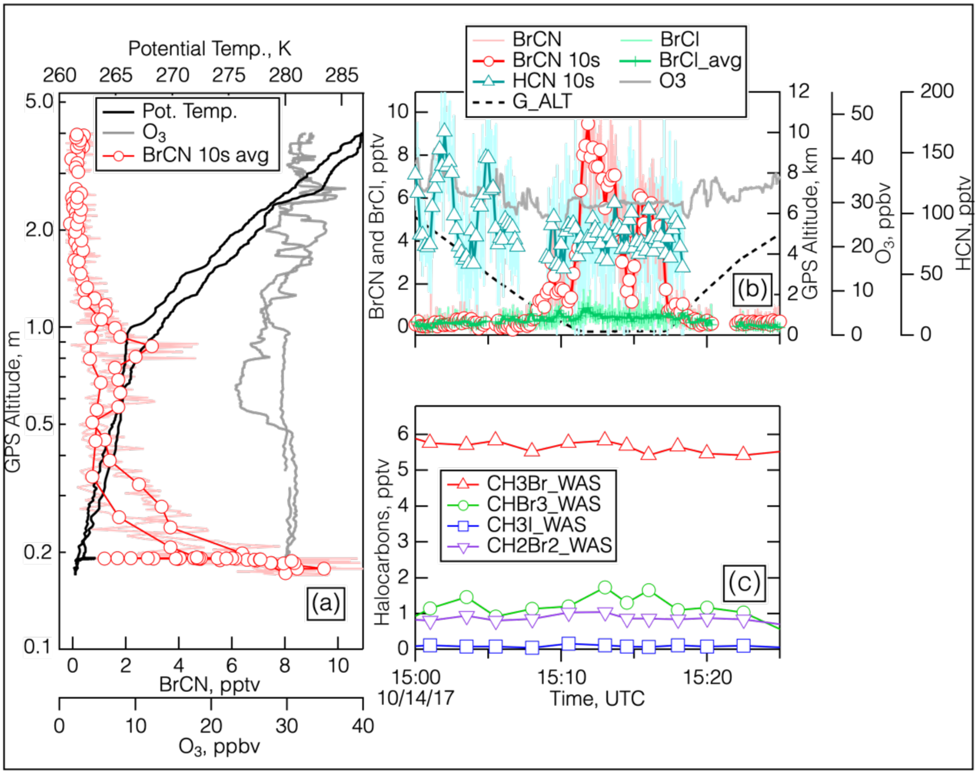

Figure S10. Details of the measurements during the polar boundary layer leg of the Oct. 14, 2017 flight at 68.6 S Lat., 30.6 W Long., centered around 15:15 UTC. Panel (a) shows the altitude profiles of potential temperature, O_3 and BrCN (10 s avg). Panel (b) shows the time series of BrCN, BrCl, HCN, O_3, and altitude. Panel (c) shows the time series of the halocarbons, CH_3Br, CH_3I, CH_2Br_2 and $CHBr_3$.

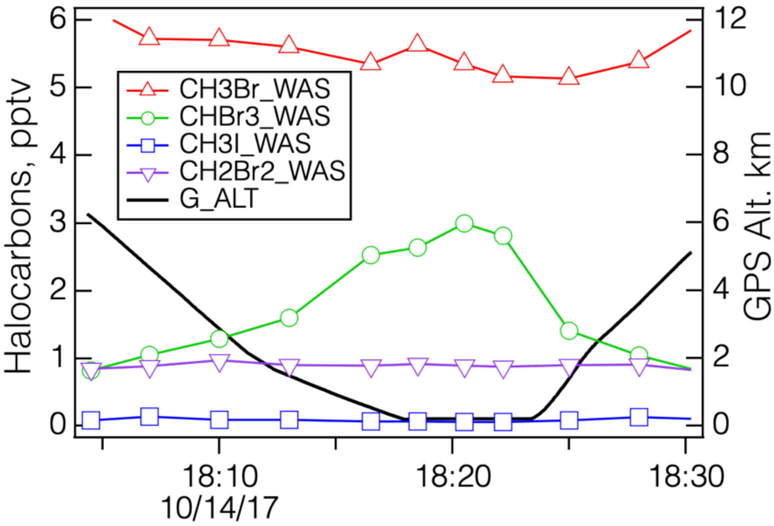

Figure S11. The time series of halocarbons, CH_3Br, CH_3I, CH_2Br_2, $CHBr_3$, and GPS altitude measured around the polar boundary layer leg centered around 18:20 during the Oct. 14, 2017 flight.

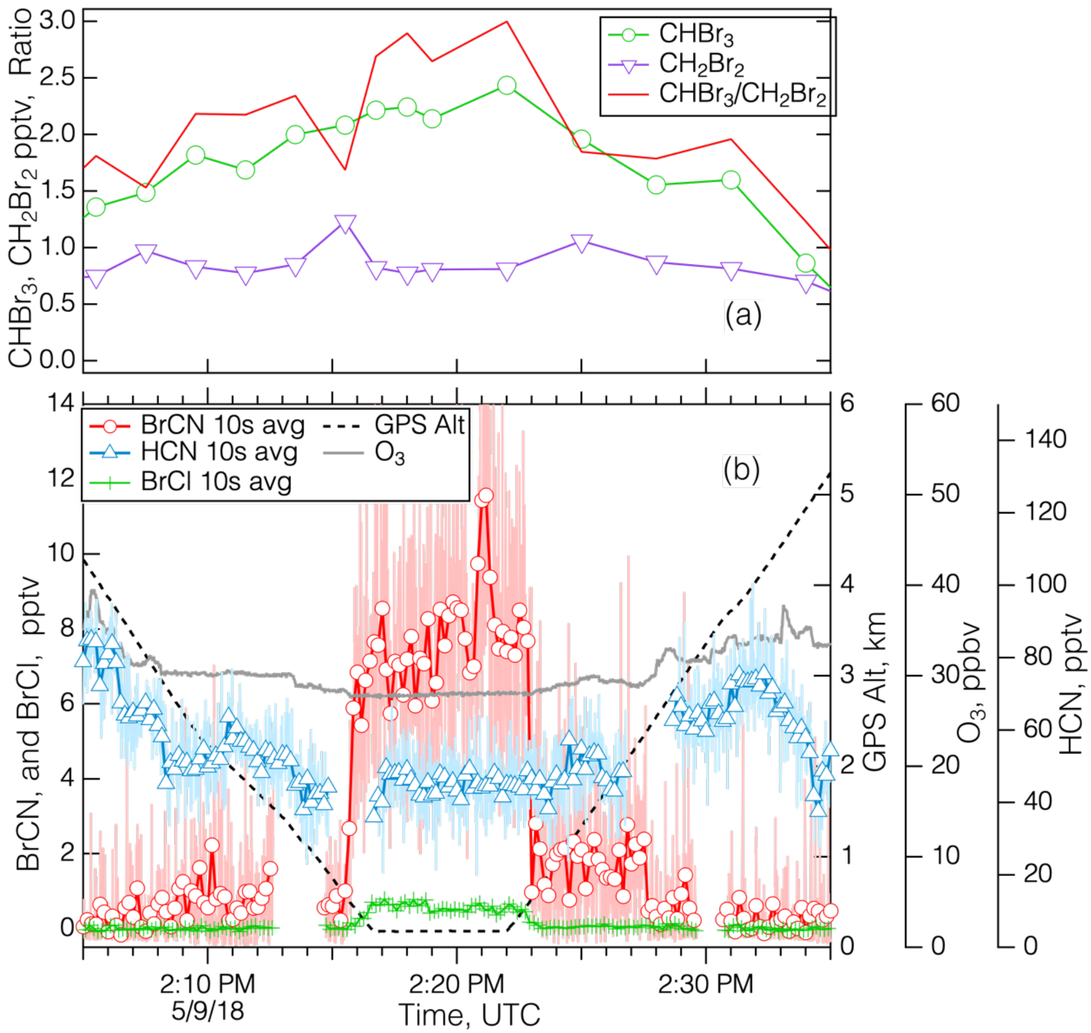

155

Figure S12. The time series of bromocarbons (Panel a) and BrCN, BrCl, HCN, O_3 and altitude (Panel b) for the first period in May, 09, 2018 when BrCN was encountered at 67.9 S Lat., 59.12 W Long..

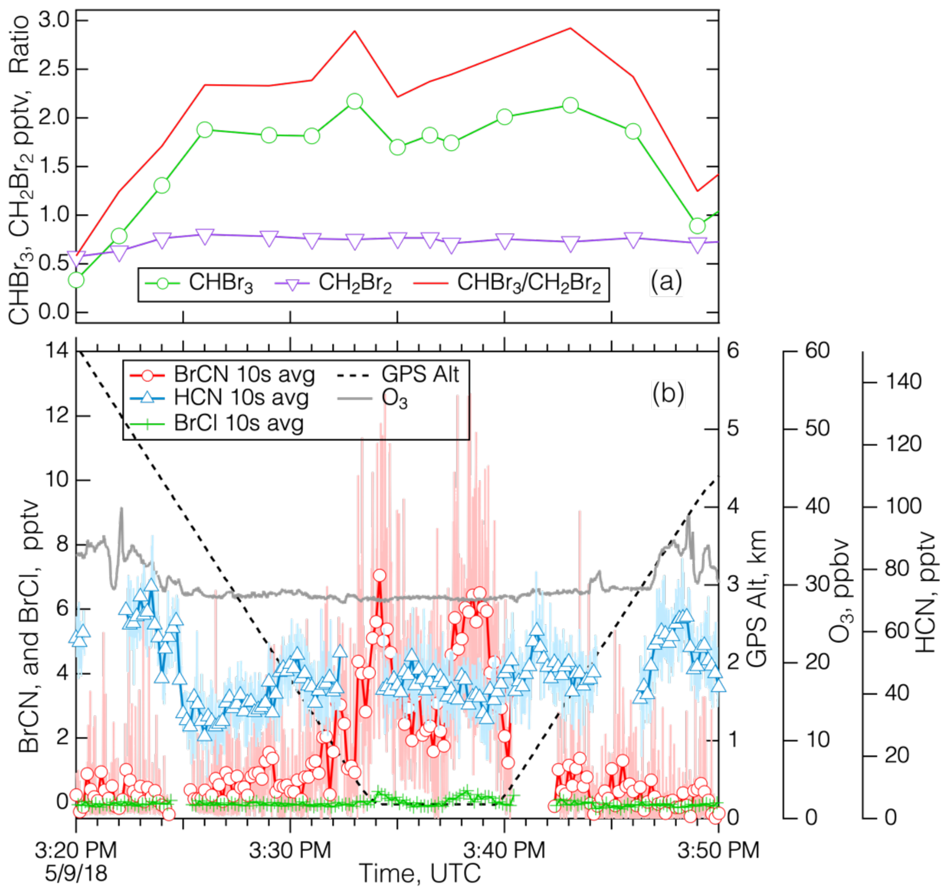

Figure S13. The time series of bromocarbons (Panel a) and BrCN, BrCl, HCN, O3 and altitude (Panel b) for the second period in May, 09, 2018 when BrCN was encountered, at 74.9 S Lat., 45.8 W Long.

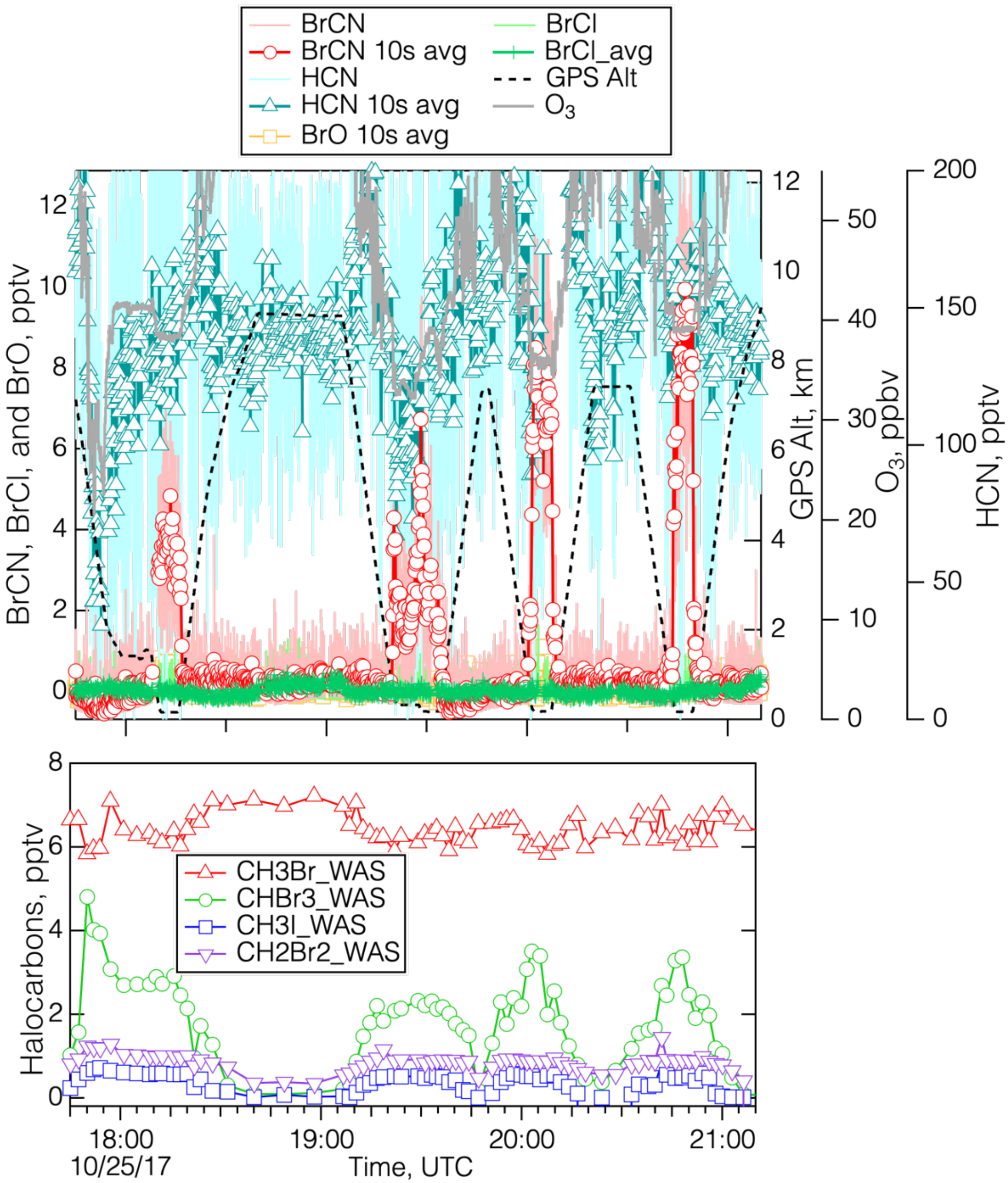

165 **Figure S14. Details of the measurements during the polar boundary layer legs of the Oct. 25, 2017 flight when BrCN above detection limit was observed. The 18:15 profile was at 74.0 N Lat., 84.6 W Long., the 19:25 profile was at 79.2 N Lat., 110.1 W Long., the 20:05 profile was at 78.7 N Lat., 125.6 W Long., and the 20:50 profile was at 75.1 N Lat., 135.5 W Long. The top panel shows the time series for BrCN, BrCl, BrO, HCN, O_3, and altitude, and the bottom panel shows the time series for the halocarbons CH_3Br, CH_3I, CH_2Br_2, and $CHBr_3$.**

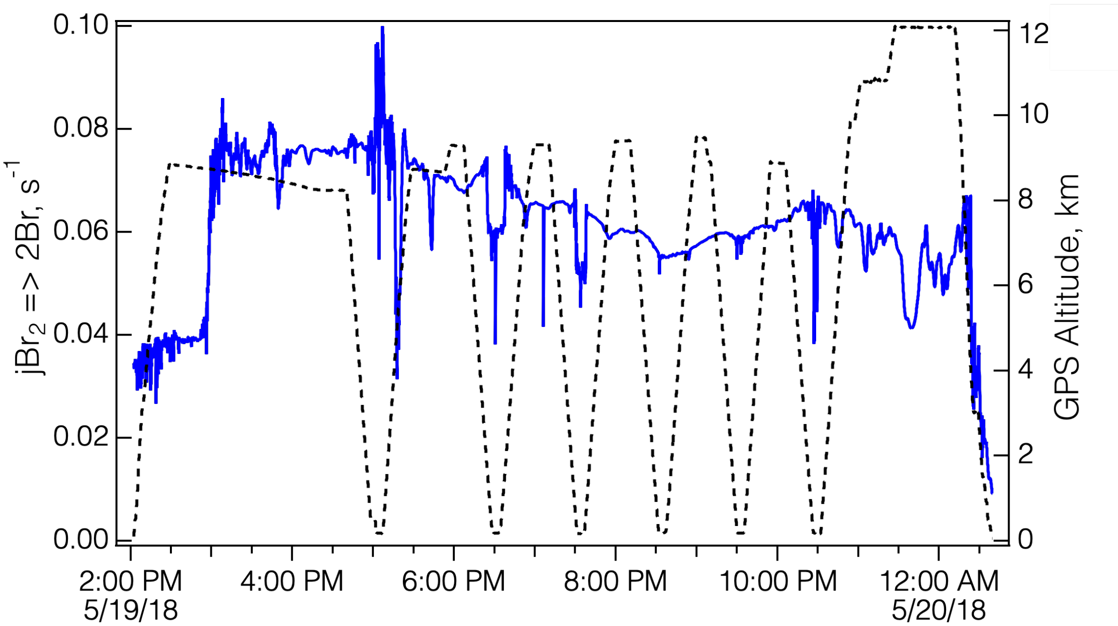

170

Figure S15. The time series of $jBr_2 \rightarrow 2\ Br$ (solid blue line) for the ATom-4 flight on May 19, 2018, plotted along with altitude (dashed black line).

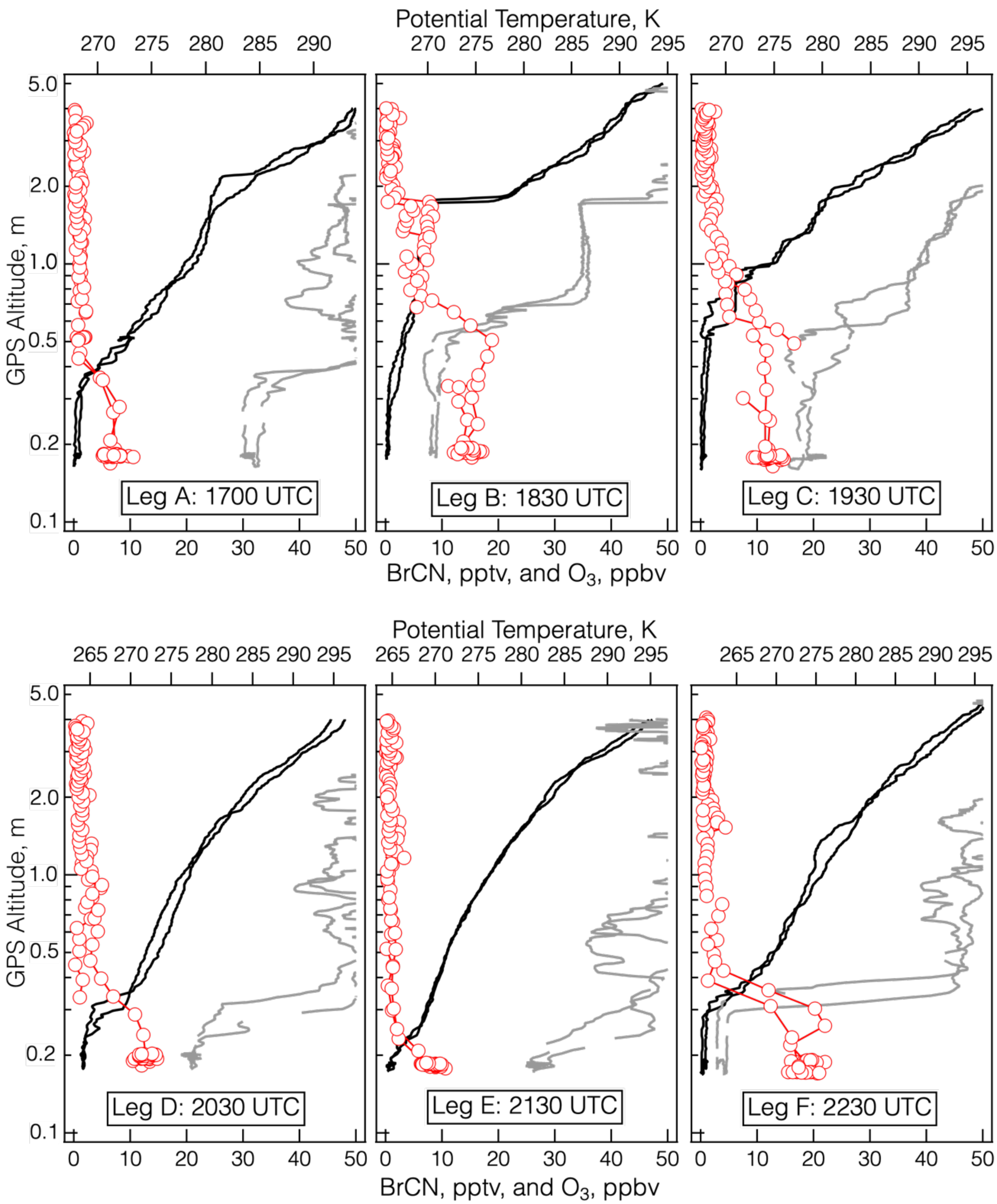

175 **Figure S16. The vertical profiles for potential temperature (black), O_3 (grey) and BrCN 10 s averages (red circles) for the 6 polar boundary layer legs during the Oct. 19, 2018 flight shown in detail in Fig. 6 and 7. Profile A was measured at 62.2° N Lat, 83.8° W Long, Profile B was measured at 70.9° N Lat, 89.5° W Long, Profile C was measured at 76.3° N Lat, 96.6° W Long, Profile D was measured at 81.4° N Lat, 110.1° W Long, Profile E was measured at 79.2° N Lat, 130.7° W Long, Profile F was measured at 73.4° N Lat, 137.6° W Long.**

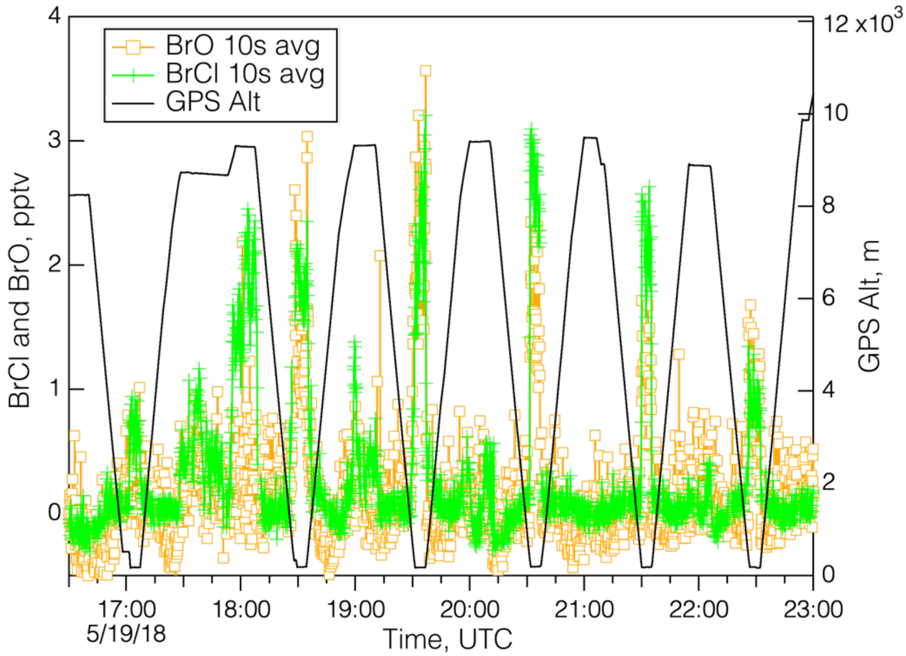

Figure S17. Measurements of BrO and BrCl during the Oct. 19, 2018 flight from Bangor, ME, to Anchorage, AK. The altitude is shown in black, BrO is shown as orange squares, and BrCl is shown as green crosses.

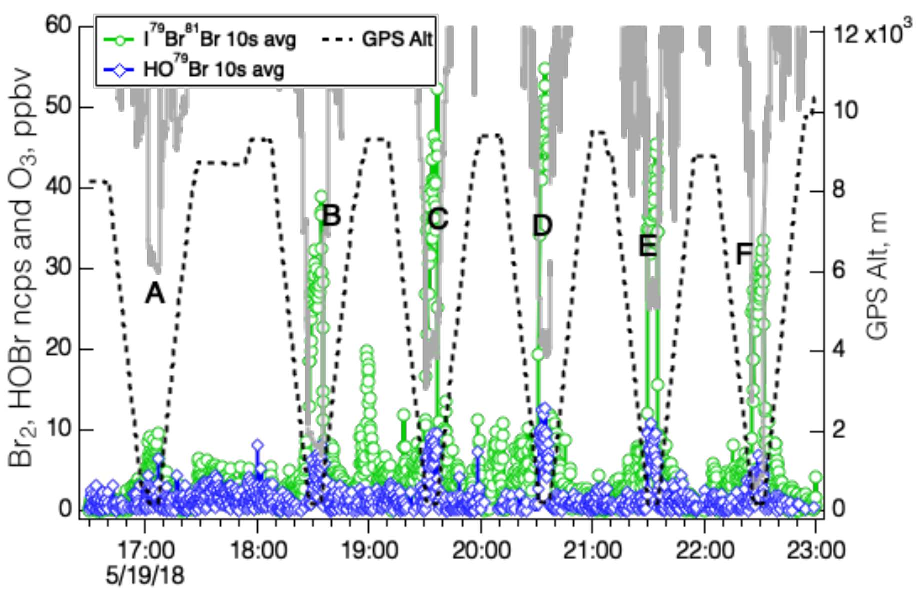

Figure S18. The time series of IBr_2^- and $IHOBr^-$ signals (in normalized counts per second) along with GPS altitude and O_3 for the flight on May 19, 2018.

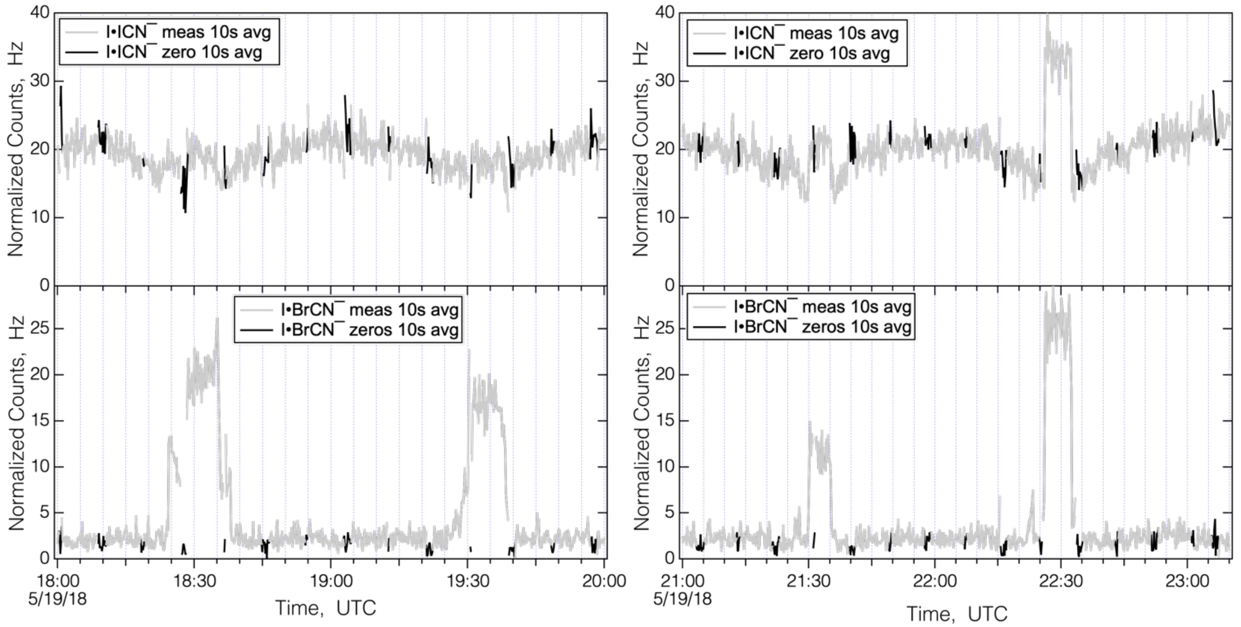

Figure S19. Comparison of the I•ICN¯ signals observed on 5/19/18 with those of I•BrCN¯. The grey lines are signals from ambient air and the black lines are signals during the periods when the inlet was overflowed with scrubbed air.

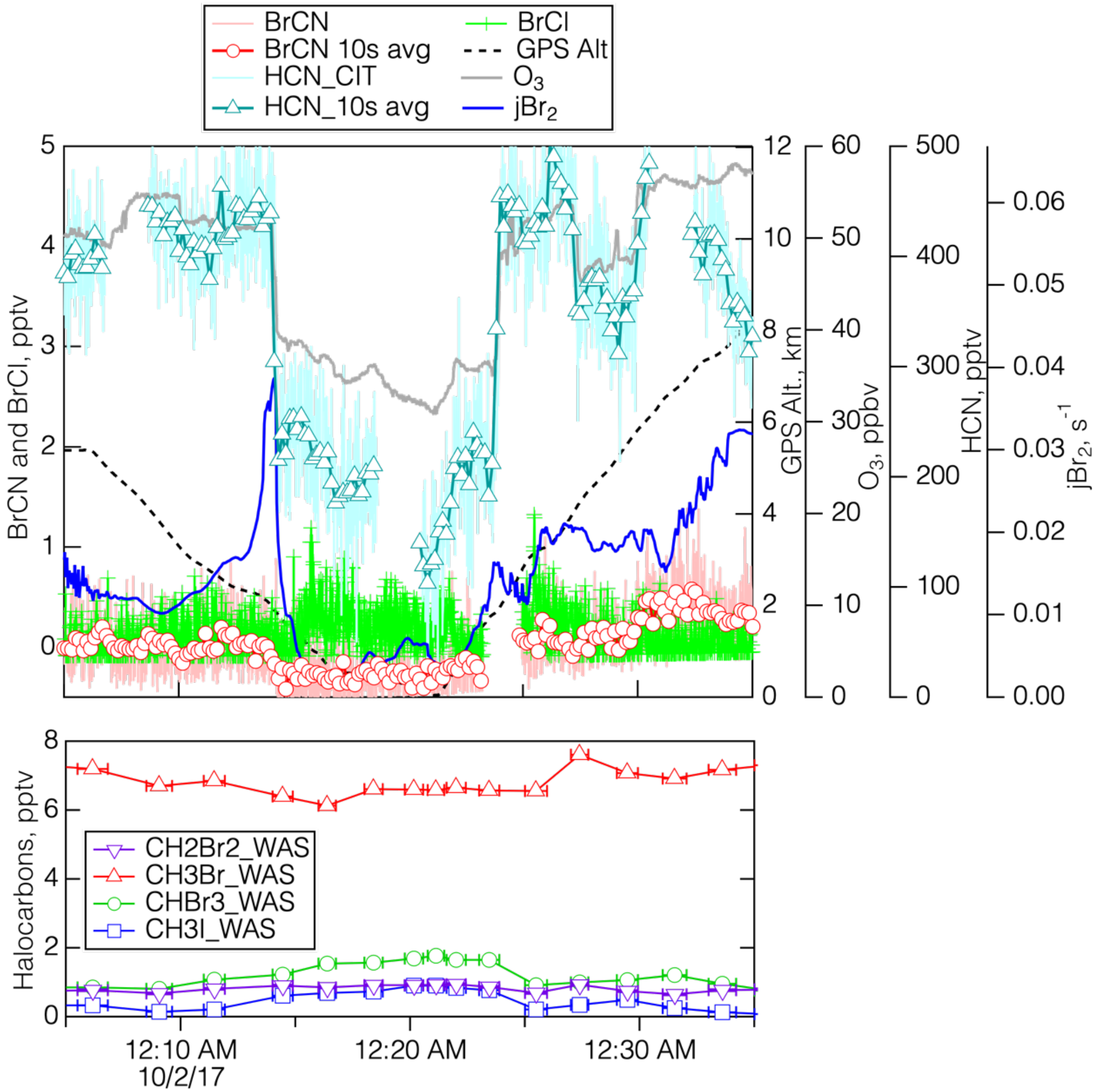

200 **Figure S20. Details of the measurements during the polar boundary layer legs of the Oct. 01, 2017 flight during the MA over BRW. The top panel shows the time series for BrCN, BrCl, HCN, O_3, jBr_2, and altitude, and the bottom panel shows the time series for the halocarbons CH_3Br, CH_3I, CH_2Br_2, and $CHBr_3$ measured by the whole-air sampler.**

Figure S21. An image from the nose camera video of the DC-8 taken at 00:20:29 (Oct. 02, 2017) UTC during the MA over BRW as part of the Oct. 01, 2017 flight described in the main text. Note the presence of low-level clouds. The videos acquired on the aircraft were stored as .mkv files (https://asp-archive.arc.nasa.gov/), converted to .avi files via MATLAB and stored on Google Drive. The videos were then played directly by Document Viewer for Google Drive.

Figure S22. The top panel shows a ©Google Earth view of BRW and the city of Utqiagvik, AK. The wind vector that corresponded to the wind direction during the lowest 2.5 km of the Apr. 27, 2018 MA is shown as the red arrow. The end of the BRW runway is very close to the shore of the Arctic Ocean, which had packed ice during the 4/27/18 MA as shown in the bottom panel taken at Apr. 28, 2018 00:35:39 from the video camera in the nose of the DC-8. The videos acquired on the aircraft were stored as .mkv files (https://asp-archive.arc.nasa.gov/), converted to .avi files via MATLAB and stored on Google Drive. The videos were then played directly by Document Viewer for Google Drive.

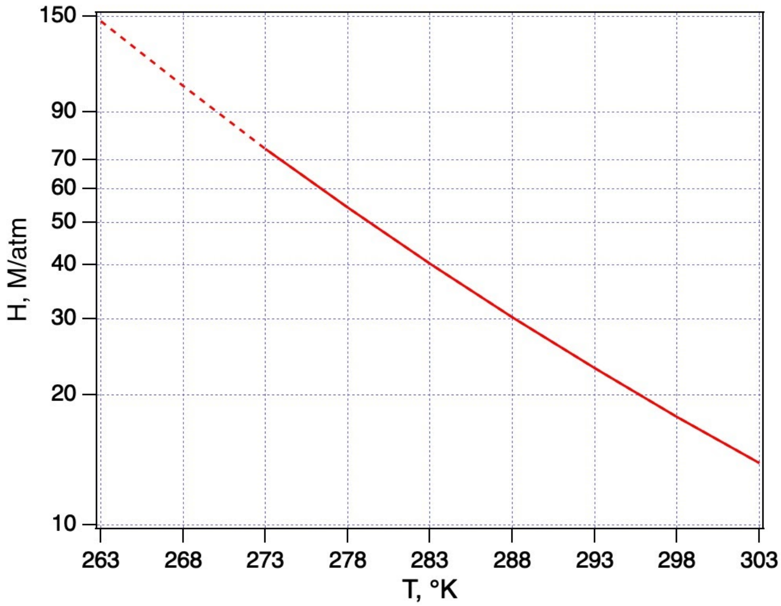

Figure S23. The Henry's Law solubility of HCN versus temperature (Yoo et al., 1986) extrapolated below the freezing point assuming that the same thermodynamic parameters apply.

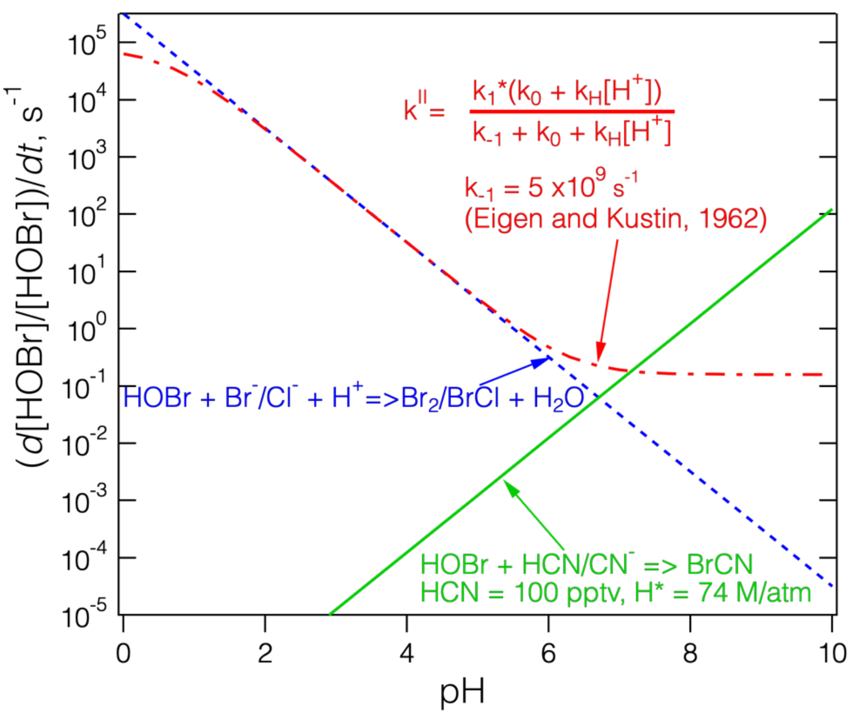

Figure S24. The relative loss rate of HOBr for either reaction with halides using either the traditional acid dependent model (blue dashed line), the acid assisted model (red dot-dashed line), or reaction with HCN/CN⁻ (green solid line) as a function of pH under the conditions specified.

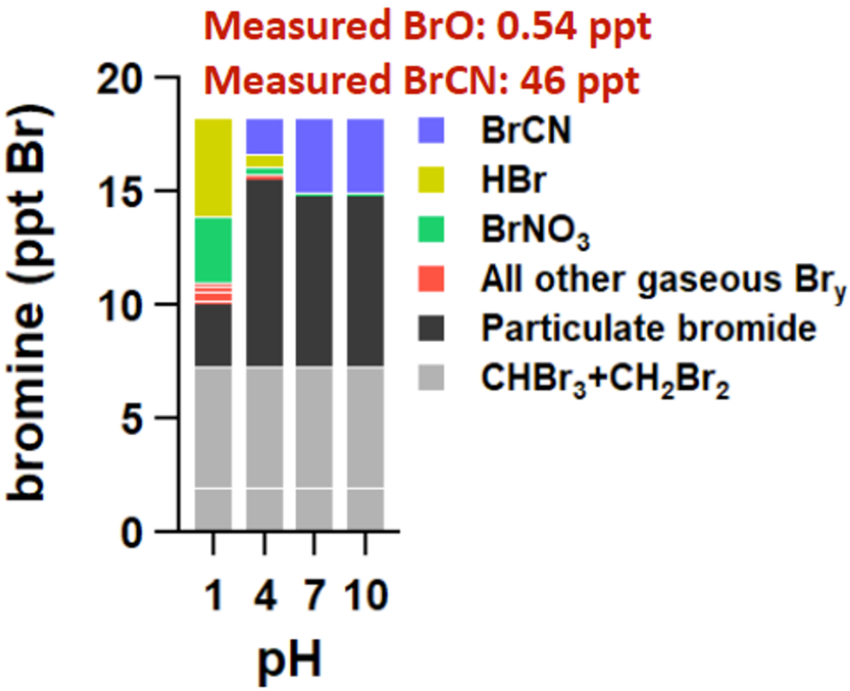

Figure S25. The result of the box model for Apr. 27, 2018 as a function of pH.

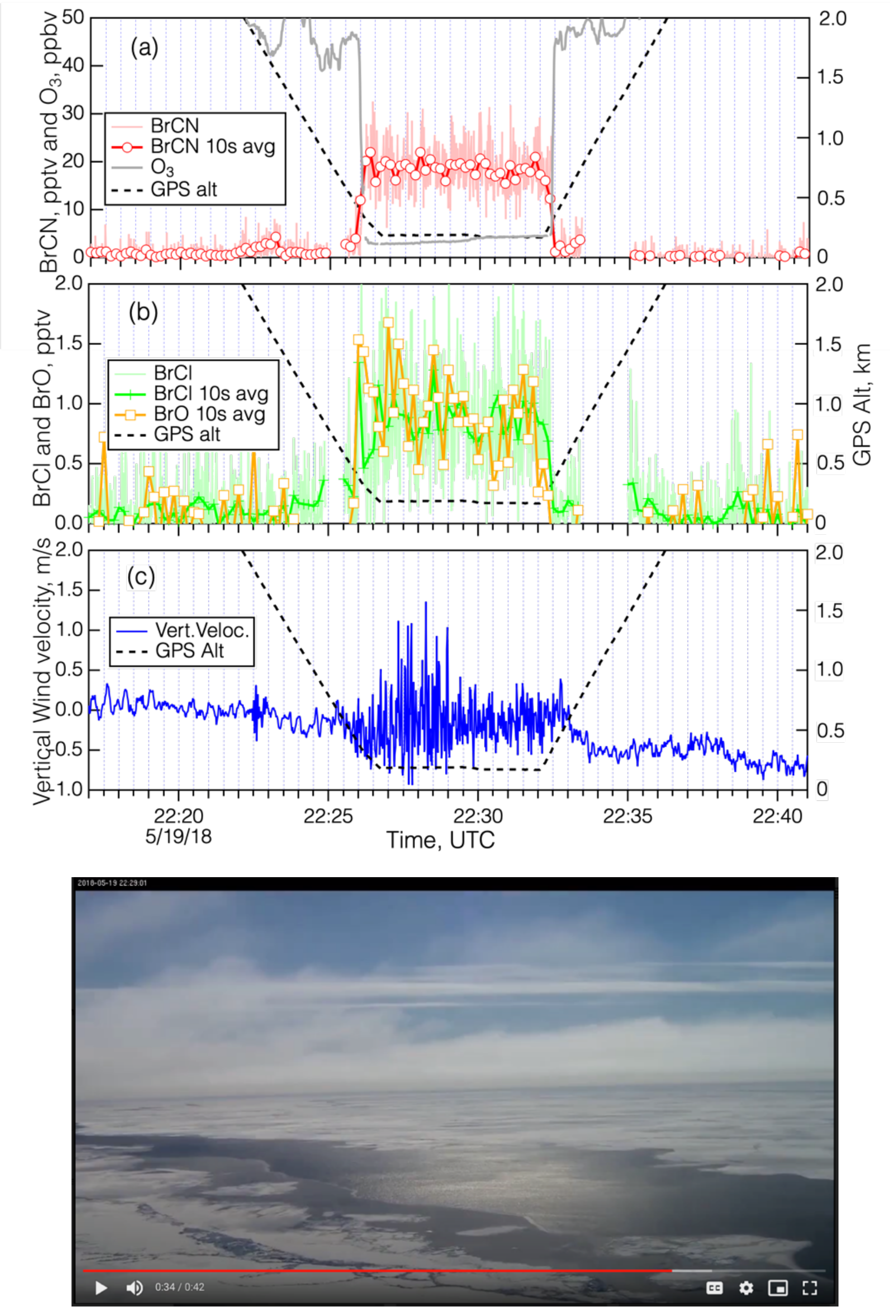

Figure S26. Details of the polar boundary layer leg on May 19, 2018, centered at 22:30 at 73.4 N Lat., and 137.6 W Long. Panel (a) shows BrCN, O_3 and GPS altitude. Panel (b) shows BrCl (1 s and 10 s avg) and BrO (10 s avg). Panel (c) shows the vertical wind velocity measured aboard the DC-8 aircraft during the polar boundary layer leg. The bottom panel is an image from the DC-8 nose video camera taken at 22:29 UTC. The videos acquired on the aircraft were stored as .mkv files (https://asp-archive.arc.nasa.gov/), converted to .avi files via MATLAB and stored on Google Drive. The videos were then played directly by Document Viewer for Google Drive.

Table S1. Properties of Cyanogen Halides, FCN, ClCN, BrCN, ICN, cyanogen (CN_2), and hydrogen cyanide (HCN), (Davis and Okabe, 1968).

Compound	Exact Mass	MP, °C	BP, °C	P_{vap}, Torr	D(X-CN), Kcal/mole†
FCN	45.0015	–	-46	Gas	111 ±0.8
ClCN	60.9719*	-6.55	13	Gas	97 ±1
BrCN	104.9214*	50–53	61–62	21 @0°C 119 @25 °C	83 ±1
ICN	152.9076	146.7	–	0.9 @25 °C	73 ±1
$(CN)_2$	52.0061	-28	-21.1	Gas	128 ±1
HCN	27.0109	-13.3	26	750 @25 °C	120 ±1

† D(C≡N) = 184 ±1

* Exact mass of the lowest isotopologue, ie., ^{35}ClCN and ^{79}BrCN.

Table S2. Halogen species measured by the I-ToF-CIMS and associated parameters. The BrCN values resulted from the comparison of the CIT-CIMS and I-CIMS data sets as described in the Methods section.

Compound	Precision, pptv	Accuracy	Detection Limit, pptv	Exact Mass
BrO	0.3	25% + 0.2 pptv	0.6	221.8183
BrCl	0.2	25% + 0.4 pptv	1.2	240.7922
Cl_2	0.2	15% + 0.4 pptv	1.2	196.8422
$ClNO_2$	0.1	15% + 0.05 pptv	0.15	207.8662
BrCN	1	25% + 0.3 pptv	1.5*	231.8264

* The detection limit for the May 12, 17, and 21, 2018 flights during ATom-4 were 6 pptv.

References

Barts, S. A., and Halpern, J. B.: Photodissociation of ClCN between 190 and 213 nm, J. Phys. Chem., 93, 7346-7351, 1989.

Davis, D. D., and Okabe, H.: Determination of bond dissociation energies in hydrogen cyanide. Cyanogen and cyanogen halides by the photodissociation method, J. Chem. Phys., 49, 5526-5531, 10.1063/1.1670082, 1968.

Dibb, J. E., Ziemba, L. D., Luxford, J., and Beckman, P.: Bromide and other ions in the snow, firn air, and atmospheric boundary layer at Summit during GSHOX, Atmos. Chem. Phys., 10, 9931-9942, 10.5194/acp-10-9931-2010, 2010.

Domine, F., Sparapani, R., Ianniello, A., and Beine, H. J.: The origin of sea salt in snow on Arctic sea ice and in coastal regions, Atmos. Chem. Phys., 4, 2259-2271, 10.5194/acp-4-2259-2004, 2004.

Felps, W. S., Rupnik, K., and McGlynn, S. P.: Electronic spectroscopy of the cyanogen halides J. Phys. Chem., 95, 639-656, 1991.

Gerritsen, C. M., Gazda, M., and Margerum, D. W.: Non-metal redox kinetics: Hypobromite and hypoiodite reactions with cyanide and the hydrolysis of cyanogen halides, Inorg. Chem., 32, 5739-5748, 10.1021/ic00077a016, 1993.

Hess, W. P., and Leone, S. R.: Absolute I* quantum yields for the ICN Ã state by diode laser gain-vs-absorption spectroscopy, J. Chem. Phys., 86, 3773-3780, 1987.

Krnavek, L., Simpson, W. R., Carlson, D., Domine, F., Douglas, T. A., and Sturm, M.: The chemical composition of surface snow in the Arctic: Examining marine, terrestrial, and atmospheric influences, Atmos. Environ., 50, 349-359, 10.1016/j.atmosenv.2011.11.033, 2012.

Li, Q., Jacob, D. J., Yantosca, R. M., Heald, C. L., Singh, H. B., Koike, M., Zhao, Y., Sachse, G. W., and Streets, D. G.: A global three-dimensional model analysis of the atmospheric budgets of HCN and CH_3CN: Constraints from aircraft and ground measurements, J. Geophys. Res. Atmos., 108, 10.1029/2002JD003075, 2003.

Quick TUV Calculator: http://cprm.acom.ucar.edu/Models/TUV/Interactive_TUV/, access: September 1, 2018, 2018.

Roberts, J. M., Osthoff, H. D., Brown, S. S., Ravishankara, A. R., Coffman, D., Quinn, P. K., and Bates, T. S.: Laboratory studies of products of N_2O_5 Uptake on Cl^- Containing Substrates, Geophys. Res. Lett., 36, L20808, 10.1029/2009GL040448, 2009.

Roberts, J. M., and Liu, Y.: Solubility and solution-phase chemistry of isocyanic acid, methyl isocyanate and cyanogen halides, Atmos. Chem. Phys., 19, 4419-4437., 2019.

Roberts, T. J., Jourdain, L., Griffiths, P. T., and Pirre, M.: Re-evaluating the reactive uptake of HOBr in the troposphere with implications for the marine boundary layer and volcanic plumes, Atmos. Chem. Phys., 14, 11185-11199, 10.5194/acp-14-11185-2014, 2014.

Russell, J. A., McLaren, I. A., Jackson, W. M., and Halpern, J. B.: Photolysis of BrCN between 193 and 266 nm, J. Phys. Chem., 91, 3248-3253, 1987.

Sander, R.: Compilation of Henry's law constants (version 4.0) for water as solvent, Atmos. Chem. Phys., 15, 4399-4981, 10.5194/acp-15-4399-2015, 2015.

Wang, S., and Pratt, K. A.: Molecular halogens above the Arctic snowpack: Emissions, diurnal variations, and recycling mechanisms, J. Geophys. Res. Atmos., 122, 11,991-912,007, 10.1002/2017JD027175, 2017.

Yoo, K.-P., Lee, S. Y., and Lee, W. H.: Ionization and Henry's Law constants for volatile, weak electrolyte water pollutants, Korean J. Chem. Eng., 3, 67-72, 10.1007/BF02697525, 1986.